INTERFACE

rsif.royalsocietypublishing.org

Research

Cite this article: Amador GJ, Mao W, DeMercurio P, Montero C, Clewis J, Alexeev A, Hu DL. 2015 Eyelashes divert airflow to protect the eye. *J. R. Soc. Interface* **12**: 20141294. http://dx.doi.org/10.1098/rsif.2014.1294

Received: 21 November 2014
Accepted: 29 January 2015

Subject Areas:
biophysics

Keywords:
porous, filter, bristles, evolution

Author for correspondence:
David L. Hu
e-mail: hu@me.gatech.edu

Electronic supplementary material is available at http://dx.doi.org/10.1098/rsif.2014.1294 or via http://rsif.royalsocietypublishing.org.

THE ROYAL SOCIETY
PUBLISHING

Eyelashes divert airflow to protect the eye

Guillermo J. Amador[1], Wenbin Mao[1], Peter DeMercurio[1], Carmen Montero[1], Joel Clewis[1], Alexander Alexeev[1] and David L. Hu[1,2]

[1]George W. Woodruff School of Mechanical Engineering, and [2]School of Biology, Georgia Institute of Technology, Atlanta, GA, USA

Eyelashes are ubiquitous, although their function has long remained a mystery. In this study, we elucidate the aerodynamic benefits of eyelashes. Through anatomical measurements, we find that 22 species of mammals possess eyelashes of a length one-third the eye width. Wind tunnel experiments confirm that this optimal eyelash length reduces both deposition of airborne particles and evaporation of the tear film by a factor of two. Using scaling theory, we find this optimum arises because of the incoming flow's interactions with both the eye and eyelashes. Short eyelashes create a stagnation zone above the ocular surface that thickens the boundary layer, causing shear stress to decrease with increasing eyelash length. Long eyelashes channel flow towards the ocular surface, causing shear stress to increase with increasing eyelash length. These competing effects result in a minimum shear stress for intermediate eyelash lengths. This design may be employed in creating eyelash-inspired protection for optical sensors.

1. Introduction

The eye is exposed, making it vulnerable to viral, bacterial, fungal and parasitic infections and their associated medical conditions. One of the most common is allergic conjunctivitis, or 'pink eye', which chronically affects up to 40% of the general population [1]. Pink eye is contracted by an assortment of airborne particles like pollen, animal dander, dust mites or droplets spread through sneezing and coughing. It is commonly believed that the eye's only line of defence is its sophisticated tear duct system which provides a thin composite layer of mucus, oil and water to lubricate the eyelid, hydrate the cornea and remove particles deposited onto the eye [2]. Beyond this system, however, little is known of the eye's other forms of protection such as the eyelashes.

Eyelashes, shown in figure 1*a–c*, are an array of bristles located at the circumference of the eye. There are many theories for the purpose of eyelashes. They are speculated to act as 'dust catchers' to protect the eye from dust falling from above [3]. Others suggest they act as sensors, similar to rat whiskers. Triggering the eyelashes or fur surrounding the eye causes the eyes to blink, protecting against nearby foreign objects [4]. In humans, eyelashes are suggested to help draw attention to the eyes and enable communication of expression [5]. In hornbills, lash-like feathers surround their eye and help shield the eye from sunlight [6].

A number of intriguing medical studies suggest that eyelashes can prevent the transfer of infection and allergens to the eye, although a clear mechanism does not exist. According to the American Optometric Association, the medical ailments alopecia and madarosis, or the lack of eyelashes, have been correlated with higher rates of infection of the eye [7]. One study found that growth of eyelashes occurs in response to exposure to allergens. Children with allergies have 10% longer and denser lashes than those without allergies [8]. This response arises from allergens triggering mast cells within the inside of the eyelid to release prostaglandins that promote hair growth [8,9], which presumably protects the eye. A missing link within this picture is the mechanism by which longer lashes reduce particle deposition.

In this study, we investigate how eyelashes affect incoming airflows. We use a range of approaches, presented in §2, including comparative anatomy, wind tunnel testing, and aerodynamic theory and numerical simulation. In §3, we

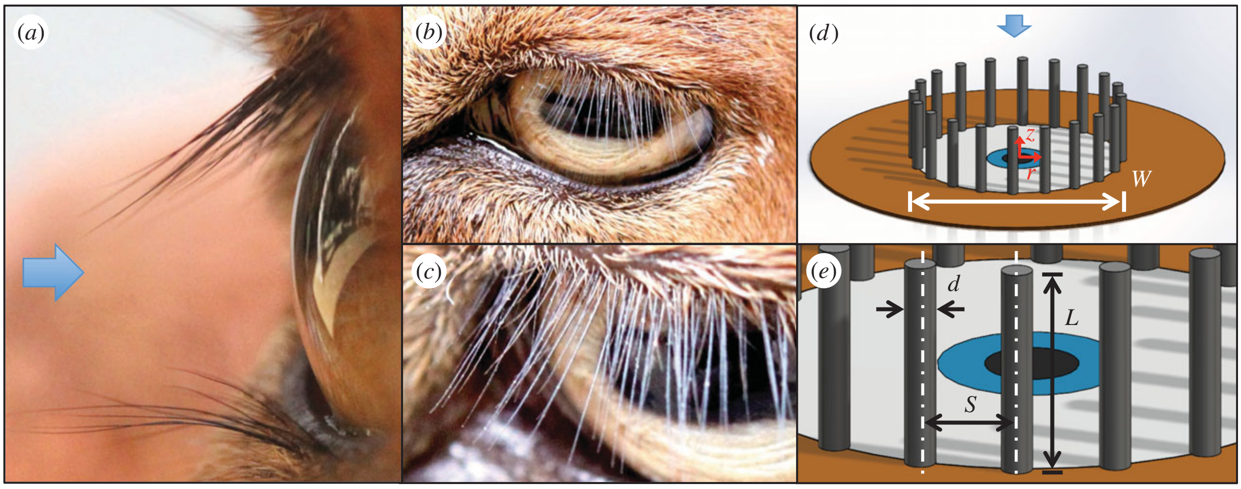

Figure 1. The mammalian eye. (*a–c*) The eye of a goat, *Capra aegagrus hircus*, including (*a*) a side-view, (*b*) a plan view and (*c*) a close-up of the eyelashes. (*d–e*) Schematics of the circular, flat eye used in our experiments, simulations and theoretical models. (*a*,*d*) Arrows indicate the direction of incoming flow, normal to the eye surface. (Online version in colour.)

present our results from these investigations. In §4, we discuss implications of our work and in §5 suggest directions for future research.

2. Material and methods

2.1. Wind tunnel experiments

We design and build a small wind tunnel, shown in figure 2*a*, capable of re-creating flows around the eye. The wind tunnel consists of a DC-powered computer fan pushing air through a diffuser followed by a laminarizer, settling chamber, nozzle and lastly the testing chamber, consisting of a cylindrical duct with a diameter of 100 mm. The flow around the eye is characterized by the ratio of inertial to viscous forces, or the Reynolds number, defined as $Re = UW/\nu$, where U is the air velocity, W is the eye width and ν is the kinematic viscosity of air. We set out airflow velocity such that $Re = 500\text{–}1000$, which, as will be discussed in §3.1, is within the range of Reynolds numbers experienced by the eyes of animals.

We also build mimics of the mammalian eye, figure 2*a*, to be tested in the wind tunnel. The eye mimic consists of an aluminium dish of depth 4 mm and diameter $W = 20$ mm, comparable to that of an adult human eye. The eye mimic sits atop a circular acrylic plate with diameter $D = 40$ mm that imitates the rest of the animal's face. Acrylic annuli are stacked around the eye, making the 'face' flush with the rim of the aluminium dish. We use a series of eyelash-mimics including mesh and commercially available eyelashes. Commercially available eyelashes made with human hair produce similar results to our eyelash mesh. As mesh is easier to fabricate, we use it in our study. If eyelashes are curved, their length is given by their vertical height rather than their arclength.

2.2. Measuring evaporation

The eye is placed in the testing chamber atop a 10^{-5} g precision scale (Mettler Toledo NewClassic MF, Model MS205DU), with the eye facing the incoming flow. We fill the aluminium dish with water to simulate the eye surface covered with the tear film. A computer connected to the scale takes automated mass readings every 10 s during a trial of 10 min, resulting in 60 total readings per trial. Average evaporation rate is found using least-squares linear regression.

Trials are run without any airflow to find the control rate of water evaporation, 4.8 μg s^{-1}. This value is subtracted from our measured evaporation rates to ensure the rates reported result exclusively from the incident flow. The trials were run indoors over a series of weeks in the summer of 2012 in a room of temperature $T = 21.5 \pm 0.5°$C and relative humidity at RH $= 46 \pm 2\%$. The small variance in temperature and humidity allowed for accurate measurements of evaporation rate.

2.3. Measuring particle deposition

We seed the incoming flow from the fan with the outflow of a commercial humidifier. The wind tunnel pushes air of density 1.16 kg m^{-3} and volumetric flow rate 3.14×10^{-3} m^3 s^{-1} into the wind tunnel; the humidifier generates a volumetric flow rate of 2.07×10^{-8} m^3 s^{-1}. This volumetric flow rate corresponds to a flow of 3.95×10^7 drops per second as the humidifier produces drops with a diameter of 10 μm. Because of the negligible volumetric flow rate provided by the humidifier, the mass flow rate striking the sample is 3.14×10^{-3} m^3 s^{-1}, with a water drop concentration of 12.6 drops mm^{-3}, or a very heavy fog [10]. This particle-laden flow is injected into the air stream through the air-guiding duct of the wind tunnel. The aluminium dish previously used to mimic the eye surface is reversed in order to expose the bottom surface of the dish to the incoming flow. A circular disc made of absorbent paper is taped to the surface to intercept the incoming flow of drops. The 10-μm diameter drops generated by the humidifier are composed of a caracin–water mixture with a ratio of 0.3 g of caracin to 2 l of water. Upon illumination by UV light and viewing through a UV light filter, the drops fluoresce.

The eye mimic is photographed with a camera (Canon 50D DSLR, 65 mm macro lens) before and after wind tunnel testing. Three trials of 10 min each were conducted for each eyelash length ($\bar{L} = L/W = 0.0, 0.1, 0.2, 0.4$ and 0.8). We use MATLAB image analysis toolbox to measure green spectrum intensity I of the photographs, examples of which are given in figure 2*b*. Photographs are imported into MATLAB and converted to matrices of RGB intensities at each pixel position. The green intensities I_i are averaged across N number of pixels of the mimic area, yielding an average intensity $I = \sum_{i=1}^{N} I_i/N$. We report intensity $I(t, \bar{L})$ as a function of both time t, in minutes, and eyelash length $\bar{L}$ using the notation $I(t, \bar{L})$. The change in intensity over the experiment may be written as

$$\Delta I(10, \bar{L}) = I(10, \bar{L}) - I(0, \bar{L}). \tag{2.1}$$

We record the change in intensity given by equation (2.1) for various eyelash lengths. This change in intensity represents the number of deposited particles.

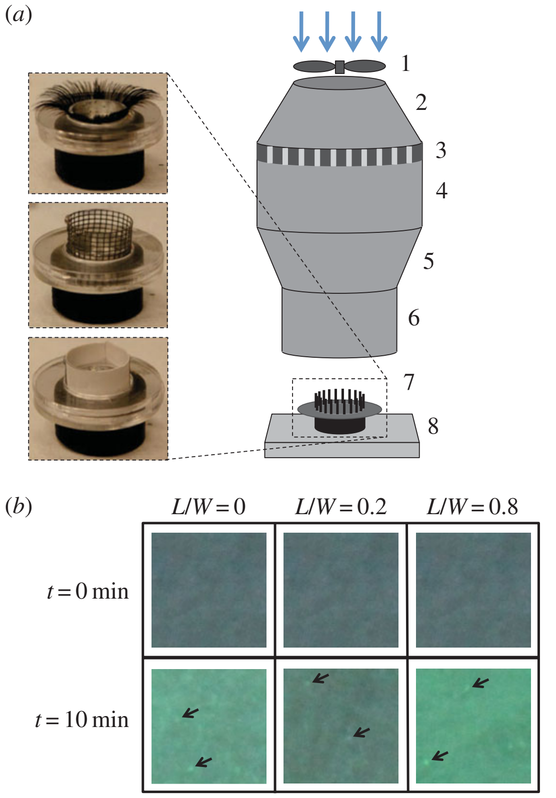

Figure 2. Wind tunnel experiments. (*a*) Eyelash mimics, from top to bottom, include human-hair eyelashes, synthetic mesh wall and impermeable paperboard. Schematic of eyelash mimic in wind tunnel. Parts include: (1) DC-powered fan, (2) diffuser, (3) honeycombed laminarizer, (4) settling chamber, (5) nozzle, (6) air-guiding duct, (7) eye mimic and (8) analytical balance. (*b*) Images showing a 1-mm^2 area of the eye mimic before and after exposure to a particle-laden flow exposure. Black arrows indicate deposited drops. (Online version in colour.)

To find the relationship between intensity and number of drops deposited, the lashless mimic is exposed to the particle-laden flow for various durations. Photographs are taken at $t = 0$, 2, 5, 7 and 10 min. Deposited drops with diameters of 10 µm are counted for five different 1-mm^2 areas on the eye mimic. The change in intensity, defined as $\Delta I(t, 0) = I(t, 0) - I(0, 0)$, is measured and correlated to the number of drops n per unit mm^2. The number of drops n increase with green intensity ΔI, indicating green intensity provides a metric for measuring the concentration of drops deposited onto the eye mimic.

In comparing intensities across eyelash lengths, we normalize with respect to our control experiment, an eye with no lashes

$$\overline{\Delta I}(10, \bar{L}) = \frac{I(10, \bar{L}) - I(0, \bar{L})}{I(10, 0) - I(0, 0)}. \tag{2.2}$$

2.4. Modelling flow around eyelashes

We may investigate the airflow surrounding eyelashes by considering the velocity distribution of fluid striking an infinite plane, shown in figure 3*a*, also known as the potential flow solution for axisymmetric stagnation point flow. This is a classical solution in the field of fluid mechanics, but for completeness we present it here. Details of the solution may be found in Panton [11] and Schlichting [12]. This solution assumes the flow is inviscid. As the boundary layer thickness for viscous axisymmetric stagnation point flow is on the order $L/W \sim 0.10$ [12], eyelashes protrude well above the boundary layer on the eye. Therefore, the assumption of inviscid flow is valid for our investigation into the flow above eyelashes.

We consider cylindrical coordinates for which the velocity field is given by $\mathbf{u} = (u_r, u_\theta, u_z)$. For steady, incompressible flow with rotational symmetry such that $u_\theta = 0$, conservation of mass may be written: $\partial u_r/\partial r + u_r/r + \partial u_z/\partial z = 0$. We solve this equation using two boundary conditions. Fluid cannot penetrate the eye surface: $u_z = 0$ for $z = 0$. Symmetry also dictates that $u_r = 0$ for $r = 0$. The velocity field that satisfies these requirements, which can be found in Schlichting [12], is

$$u_r(r) = ar, \quad u_\theta = 0 \quad \text{and} \quad u_z(z) = -2az, \tag{2.3}$$

where a is a real constant found to be $a = 5.7\ \mathrm{s}^{-1}$ using our numerical methods to find the radial velocity u_r as a function of radial position r. As lashes increase in length, the vertical velocity magnitude of the flow entering the eyelash array increases according to $|u_z(L)| = 2aL$.

2.5. Modelling flow at eye surface

For the airflow close to the eye surface, viscosity dominates and a boundary layer is formed. Unlike the flow above the eyelashes, the flow inside the boundary layer cannot be treated as inviscid. This is another classical solution in the field of fluid mechanics, which was first reported by Hiemenz [13]. For completeness, we will present it here, following Schlichting [12]. In order to model the flow, we choose our domain to be inside the boundary layer, where $z = 0$ at the eye surface and $z = \infty$ at the upper bound of the boundary layer where the flow velocity follows potential flow theory, equation (2.3). For the viscous boundary layer in axisymmetric stagnation point flow mass conservation: $\partial u_r/\partial r + u_r/r + \partial u_z/\partial z = 0$, and momentum conservation in r

$$u_r\frac{\partial u_r}{\partial r} + u_z\frac{\partial u_r}{\partial z} = -\frac{1}{\rho}\frac{\partial p}{\partial r} + \nu\left(\frac{\partial^2 u_r}{\partial r^2} + \frac{1}{r}\frac{\partial u_r}{\partial r} + \frac{u_r}{r^2} + \frac{\partial^2 u_r}{\partial z^2}\right)$$

give the governing equations for the flow dynamics [12]. Here, ν is the kinematic viscosity of air and ρ its density. We solve these two equations using three boundary conditions. Fluid cannot penetrate the eye surface: $u_z = 0$ for $z = 0$. As the flow is viscous, there is zero radial velocity at the eye surface: $u_r = 0$ for $z = 0$ (no-slip). At the upper bound of the boundary layer, the radial velocity is equal to the free stream potential flow velocity: $u_r = ar$ for $z = \infty$.

In order to solve these governing equations, the following forms of the velocity and pressure profiles are assumed: $u_r = rf'(z)$, $u_z = -2f(z)$ and $P_0 - P = 1/2\rho a^2[r^2 + F(z)]$. Here, $F(z)$ is a function dictating the variation in pressure P as a function of the distance z away from the eye, and P_0 is the ambient pressure. For our purposes, the function $F(z)$ does not need to be determined as we are only interested in the velocity field, u_r and u_z. This assumed form satisfies mass conservation and leads to the following differential equation for momentum conservation, $f'^2 - 2ff'' = a^2 + \nu f'''$. The boundary conditions are: $f = f' = 0$ for $z = 0$ and $f' = a$ for $z = \infty$. A similarity transformation to remove the constants in the governing equations is: $\zeta = \sqrt{(a/\nu)}z$ and $f(z) = \sqrt{a\nu}\theta(\zeta)$. This transformation yields the following differential equation for θ: $\theta''' + 2\theta\theta'' - \theta'^2 + 1 = 0$, with the boundary conditions: $\theta = \theta' = 0$ for $\zeta = 0$ and $\theta' = a$ for $\zeta = \infty$. This equation is solved numerically using MATLAB. Physically, θ can be interpreted as the dimensionless streamfunction [12].

2.6. Modelling flow through eyelashes

To investigate flow through the eyelashes, we model the lashes as a linear array of cylinders [14,15]. Using a method first proposed by Keller [14], the pressure drop across the array can be simplified to that between a pair of cylinders of diameter d and centre-to-centre spacing S. We consider two-dimensional flow in the x-direction, as shown in figure 3*b*. The gap between the cylinders can be written as twice the height $h(x) = S/2 - \sqrt{(d/2)^2 - x^2}$.

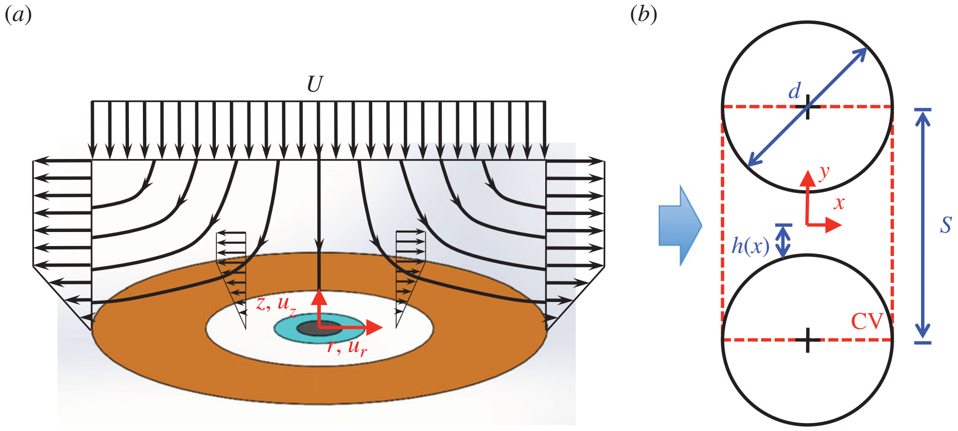

Figure 3. Modelling flow through eyelashes. (*a*) Streamlines in the $r-z$ plane associated with potential stagnation point flow with a linear boundary layer. (*b*) Geometry used in viscous flow analysis to determine an expression for the pressure drop ΔP across an array of eyelashes. The control volume is defined by the dashed rectangle, and the incoming airflow (arrow) flows through the gap between cylindrical lashes with diameter d. The centre-to-centre distance between lashes is defined as S and is assumed to be $S \approx d$, where d is the lash diameter. (Online version in colour.)

In the limit that the local Reynolds number $Re_d = (Ud/\nu) < 1$, where U is the incoming air velocity and ν is the kinematic viscosity of air, we may apply Stokes' law. For flow between lashes, the fluid velocity follows a parabolic profile similar to that between two parallel plates, or $u(x) = P_x/2\mu[y^2 - h^2(x)]$. Here, P_x is the pressure gradient in the x-direction and μ is the dynamic viscosity of air. The volumetric flow rate per unit length of the lashes is $q = \int_{-h}^{h} u\,\mathrm{d}y = -2h^3P_x/(3\mu)$. Solving for P_x yields an expression for the pressure gradient: $P_x = -3\mu q/(2h^3)$. From this expression, we can find the pressure drop across the gap as: $P(-d/2) - P(d/2) = 3\mu q \int_0^{d/2} h^{-3}(x)\,\mathrm{d}x$. Assuming $S \approx d$, we use asymptotic expansion to first order to obtain $P(-d/2) - P(d/2) \approx (9\pi\mu q)/(2^{3/2}S^2(1-d/S)^{5/2})$. We may make two further simplifications. The flow velocity U_2 through the lash array is given by $q = (S-d)U_2$. The pressure drop across the gap is equal to the pressure drop across the entire eyelash array: $P(-d/2) - P(d/2) = \Delta P$. Consequently,

$$\Delta P = \frac{9\pi\mu(S-d)U_2}{2^{3/2}S^2(1-d/S)^{5/2}}. \tag{2.4}$$

2.7. Numerical methods

We employ a lattice Boltzmann model (LBM) [16–19] to examine the interactions between eyelashes, the ocular surface and the viscous flow. The LBM is a mesoscale computational model for simulating hydrodynamic flows governed by the Navier–Stokes equations. The method is based on the time integration of a discretized Boltzmann equation $g_i(\mathbf{r} + \mathbf{c}_i\Delta t, t + \Delta t) = g_i(\mathbf{r}, t) + \Omega[g(\mathbf{r}, t)]$ for a particle distribution function g. Here, $\mathbf{c}_i$ is the fluid particles' velocity in the direction i at a lattice node $\mathbf{r}$ at time t, Δt is the time step and Ω is the collision operator accounting for the change in g due to instantaneous collisions at the lattice nodes. The moments of the distribution function are used to calculate fluid density $\rho_a = \sum_i g_i$, the momentum density $j = \sum_i \mathbf{c}_i g_i$ and the stresses $\Pi = \sum_i \mathbf{c}_i \mathbf{c}_i g_i$. We use a three-dimensional 19-velocity model (3D19Q) defined on a simple cubic lattice and a multiple-relaxation-time collision operator [18].

The simulations are conducted in a rectangular computational box. Due to the axisymmetric flow nature, only a quarter of region around the eye is simulated. The box has dimensions 2.5 $W \times$ 2.5 W in the horizontal plane and 7 W in the vertical z-direction. The computational domain is discretized by 180 × 180 × 504 nodes on a uniform Cartesian grid. Symmetric boundary conditions are used in the horizontal direction and a uniform flow is imposed at top boundary. The eye and face are modelled as concentric flat discs with diameters of D and W, respectively.

We limit our simulations to the values of the laminar Reynolds number $Re = UW/\nu$ below 500. In this case, the local Reynolds number that characterizes the flow around the eyelashes, $Re_d = Ud/\nu$, is less than one. We model each eyelash in our simulations as a sequence of static beads that are uniformly distributed along its length L and experience a drag force. Here, we neglect the effect of eyelash flexibility on the emerging fluid flow. Frictional force in the form of $\mathbf{F}_\mathrm{f} = -\xi\mathbf{u}_\mathrm{f}$ is used to account for the effect of eyelashes on the flowing air [20,21]. Here, $\mathbf{u}_\mathrm{f}$ is the local fluid velocity and ξ is the drag coefficient [22]. The frictional force is distributed to LBM nodes surrounding the beads constituting the eyelash using a delta function [23]. Interpolated bounce-back rule is used to impose a no-slip and no-penetration boundary conditions at the ocular surface [24].

The effective radius of eyelash and the spacing s between the beads in each eyelash are determined based on simulations of a flow passing through an infinitely long cylinder that were compared to Lamb's solution [25]. This solution agrees with experimental data up to a Reynolds number of $Re_d = 1$ [26,27]. We find that by tuning the ratio of eyelash diameter and the spacing between the beads s/d, the drag coefficients obtained in these simulations were within 5% error compared with Lamb's solution. In our simulations with different eye Reynolds numbers Re, we measure the average Reynolds number of an eyelash Re_d and set the spacing s/d to minimize the simulation error. Specifically, for $Re_d = 0.55$ (corresponding to $Re = 500$), we use $s/d = 0.5$; for $Re_d = 0.27$ (corresponding to $Re = 250$), we use $s/d = 0.8$; for $Re_d = 0.16$ (corresponding to $Re = 150$), we use $s/d = 1.1$.

We have previously extensively validated LBM and applied it to study flows near solid surfaces covered with hair-like filaments in the limit of small Reynolds numbers [28–31]. We have also used the model to simulate flows with finite Reynolds numbers near moving surfaces and particles [32–35]. Additionally, we verified that the domain size used in our simulations is sufficiently large and that its boundaries do not affect the flow around the eye. To this end, we increased the domain size by 1.5 times in all three directions. The results of this validation simulation showed that the increased domain size has a negligible effect on the flow near the eye. To examine the effect of grid resolution on the solution accuracy, we increased the grid density by 1.5 times. We found that the increased grid resolution practically does not affect the velocity field near the eye, as shown in electronic supplementary material, figure S1. Furthermore, we checked that the increased grid resolution does not affect the optimal eyelash length.

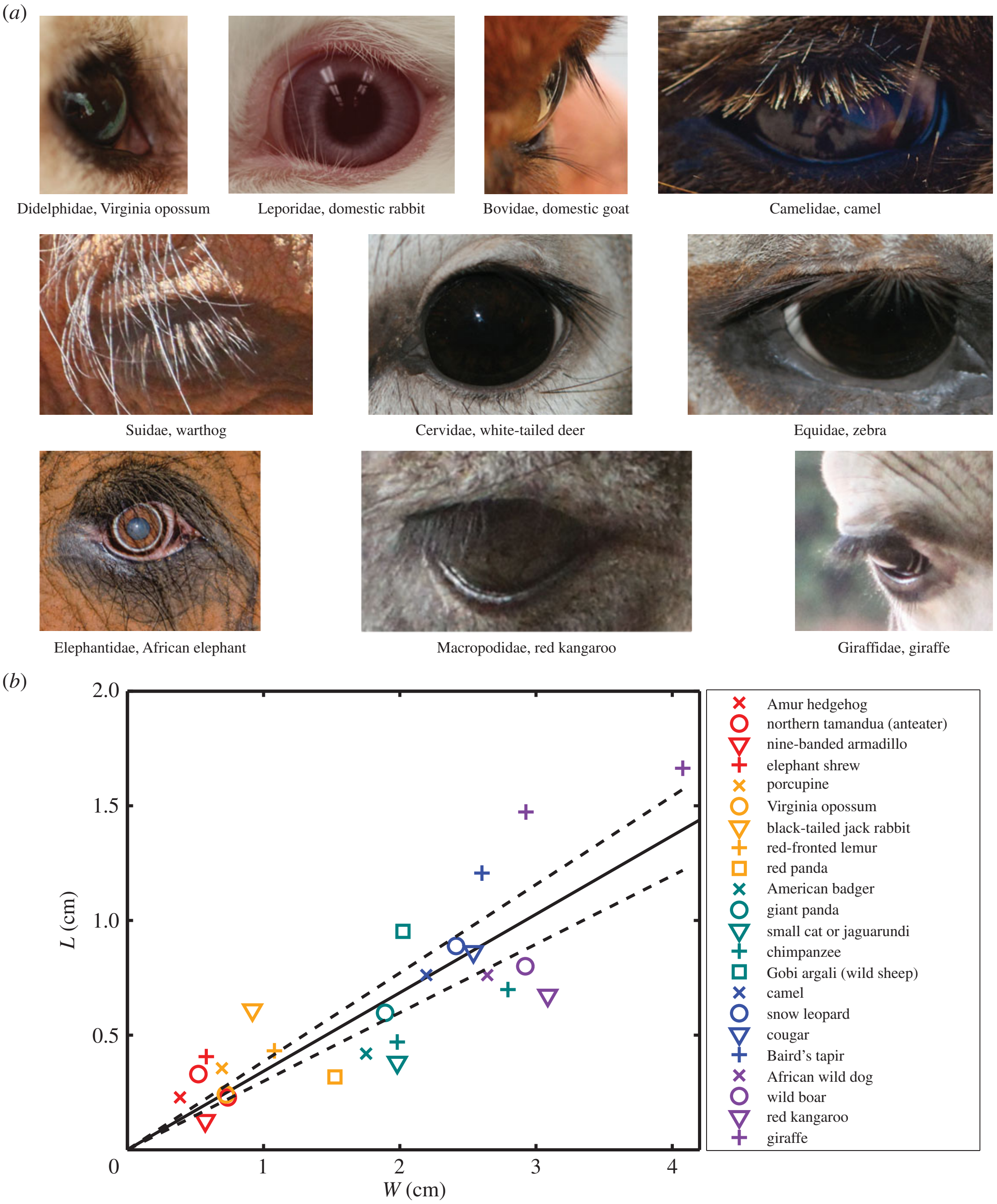

Figure 4. Eyelashes of mammals. (*a*) The eyes of a selection of mammals. Photo credits: camel by bgrimmni (Flickr), elephant by Tim Nowack and the rest belong to the authors. (*b*) Relationship between eyelash length L and eye width W for 22 species of mammals. Solid line indicates least-squares best fit and dashed lines represent the 95% CI for the linear regression. (Online version in colour.)

3. Results

3.1. Anatomical measurements

We begin with characterizing the dynamical regime of eyelashes so that we can match our experiments to that of live mammals, like those shown in figure 4*a*. The mammalian eye has width W and the lashes have length L, diameter d and centre-to-centre spacing S, as shown in figure 1*d*,*e*. The animal walks forward at speed U through air with kinematic viscosity ν. By Buckingham's theorem [36], the system is characterized by three dimensionless groups

$$Re = Re\left(\frac{UW}{\nu}, \frac{L}{W}, \frac{S}{d}\right). \tag{3.1}$$

The walking speed U is found in the literature for 12 species of animals [37–44]. The walking speed of animals ranges from $0.05\ \mathrm{m\,s^{-1}}$ for the hedgehog to $6.5\ \mathrm{m\,s^{-1}}$ for the red kangaroo. The Reynolds number $Re = UW/\nu$ ranges from 10 to 12 000 for the animal eyes depicted in figure 4*b*.

A more common dimensionless number can be derived from the dimensionless centre-to-centre gap S/d. We can define the porosity $\phi = 1 - d/S$ as the ratio of void area to total area, a common parameter used in the filtration and porous flow literature. From now on, the porosity ϕ will be used as the third dimensionless number, in place of the dimensionless gap S/d.

We use macro-photography to measure the eyelashes of 22 species of mammals, found among preserved pelts and heads at the American Museum of Natural History in New York City, NY and Broderick Head Taxidermy in Roopville, GA. Figure 4*a* shows representatives of mammals with eyelashes and demonstrates the consistency in morphological form across the otherwise phylogenetically diverse mammalian species. As the eye opening is elliptical for several species, we report W as the average of the widths along major W_1 and minor W_2 axes. In analysis of images from various image databases, we find eyelashes or fur around the eye are quite common, occurring in 87 out of 126 extant mammal families (see the electronic supplementary material).

Figure 4*b* shows the relationship between eyelash length L and eye opening diameter W,

$$\frac{L}{W} = 0.34, \tag{3.2}$$

where the goodness of the least-squares fit is $R^2 = 0.69$ based on the following definition of coefficient of determination [45]: $R^2 = 1 - \sum_i (L_i - \hat{L}_i)^2 / \sum_i (L_i - L_{\mathrm{ave}})^2$, where L_i is the measured eyelash length data for the ith animal, $\hat{L}_i$ is the predicted eyelash length following equation (3.2) for the ith animal and L_{ave} is the mean measured eyelash length. The fit is fair, considering the animals span a wide range of genetic heritage and over four orders of magnitude in weight from the Amur hedgehog to the giraffe. The 95% CI for the linear regression is represented by the dashed curves in figure 4*b* and spans the range $L/W = 0.3$–0.4.

The variability in dimensionless eyelash length L/W seems substantial, but is low compared with that found in previous studies of animal body hair. Dickerson *et al.* [10] showed there is in fact no clear relationship between body hair length and body mass for mammals. We can thus conclude that eyelash length has been tuned by evolutionary pressures far stronger than those for body hair.

Eyelash spacing does not vary systematically with eye size. For the 22 species of mammals studied, the eyelash density ρ_{lash} is restricted to $\rho_{\mathrm{lash}} = 20 - 60$ eyelashes per cm, as shown in figure 5. This range in eyelash density is comparable to body hair density (3–10^2 hairs cm^{-1}) on the same set of mammals [10]. Both eyelash and body hair density appear to be independent of animal size.

The corresponding porosity range for eyelashes is $\phi = 0.38$–0.85, according to the definition $\phi = 1 - \rho_{\mathrm{lash}} d$, where ϕ is the porosity representing the ratio of void area to total area for the wall of eyelashes, $\rho_{\mathrm{lash}} = S^{-1}$ is the number of eyelashes per unit length, and d is eyelash diameter, reported in the electronic supplementary material. We employ this range of porosities in our experiments and simulations.

The 22 mammalian species studied are phylogenetically diverse, spanning 12 orders within the class Mammalia as shown in the phylogenetic tree in figure 6*a*. Using the phylogenetic data for mammals from Bininda-Emonds *et al.* [46], we conduct a statistical analysis using the method of independent contrasts (IC) to determine if the trends found through anatomical measurements are significant upon consideration of the proximity of phylogenetic relations between species. This method uses tree structure and time from divergence to take into account relations between animal species and generates statistically independent values representative of the measurable traits of animals [47,48]. The method of IC assumes character evolution follows Brownian motion [47].

As shown in the figure 6*b*, the statistical method of IC, which takes into account mammalian phylogeny (figure 6*a*), results in a linear relation between the contrasts of length L_{IC} and width W_{IC} with a goodness of fit of $R^2 = 0.65$. The similarity in goodness of fit with that of the raw data suggests that the relationship between eyelash length L and eye width W is significant.

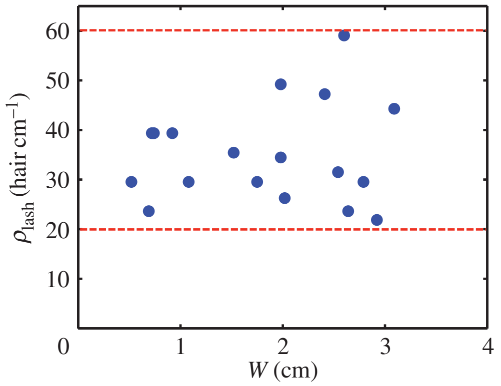

Figure 5. Eyelash density is independent of eye size. Relationship between eyelash density ρ_{lash} and eye width W. (Online version in colour.)

3.2. Scaling theory

In this section, we model the effect of an array of eyelashes on the shear stress τ at the ocular surface. The computational domain is shown schematically in figure 7*a*. Figure 7*b*–*d* shows the radial velocity profiles predicted by our model for three cases: no lashes, short lashes and long lashes. The radial velocity profiles u_r are given as a function of height z from the eye. The method for determining these profiles is discussed in turn below.

When there are no eyelashes present, shown in figure 7*b*, we may determine the thickness δ of the linear boundary layer by using the known solution for viscous stagnation point flow, as outlined by Schlichting [12] and in §2.5. This solution uses the potential flow solution, equation (2.3), as boundary conditions to determine the effects of viscosity on stagnation point flow and determine the shear stress τ_0 on the ocular surface when there are no eyelashes present. The shear stress is given by $\tau_0 = \mu(\partial u_r/\partial z)$. Using the similarity transformations in §2.5, we can get an expression for τ_0 in terms of the dimensionless streamfunction θ, or $\tau_0 = (\mu a W/4)\sqrt{a/\nu}\,\theta'''(z=0)$. The constant $\theta''(z=0)$ is found numerically following the methods in §2.5 and is also presented in the study of Schlichting [12].

In order to approximate the boundary layer as linear, we find the linear boundary layer thickness δ required to yield the same shear stress τ_0 given by the viscous stagnation point theory. For a linear velocity profile, the shear stress τ_0 at the eye surface is expressed as $\tau_0 = (\mu u_r(r = W/4))/\delta$. Here, $u_r(r = W/4) = aW/4$ is the average airflow velocity outside of the boundary layer above the ocular surface. This point was selected because it is the velocity at the point halfway between the centre and edge of the eye, given by equation (2.3). Evaluating the radial velocity at $r = W/4$ will yield the average shear stress τ_0 on the ocular surface. Using the expression for τ_0, we can find an expression for the linear boundary layer thickness,

$$\delta = \frac{\mu a W}{4\tau_0}. \tag{3.3}$$

Short eyelashes, such as the optimal lashes, shown in figure 7*c*, create a stagnation zone just above the eye surface to an amount $\delta + L$, where L is the length of the lashes. This thickening results in a shear stress, $\tau_1 = \mu u_r(r = W/4)/\delta + L$, at the ocular surface. Substituting for the velocity profile from equation (2.3) and the boundary layer thickness δ from equation (3.3), yields an expression for the shear stress τ_1 for short lashes,

$$\tau_1 = \frac{\mu a W}{(\mu a W/\tau_0) + 4L}. \tag{3.4}$$

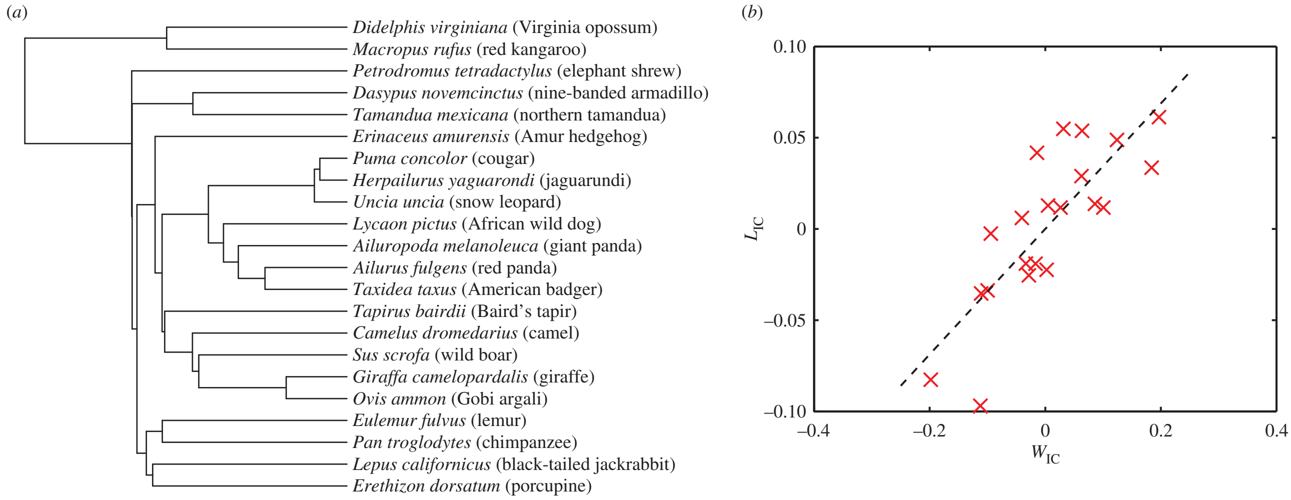

Figure 6. Phylogenetic analysis of eyelash length. (*a*) Phylogenetic tree showing the 22 mammalian species studied. (*b*) Relationship between eyelash length contrast L_{IC} and eye width contrast W_{IC}. (Online version in colour.)

For long lashes, shown in figure 7*d*, the flow enters the cylindrical volume enclosed by the eyelash array, generating a modified stagnation point flow. We model this modified flow by conserving energy between two points, the flow entering the eyelash array at $z = L$ and the flow exiting the array. These points are used to determine the radial airflow velocity U_2 leaving the eyelash array. The kinetic energy per unit volume entering the volume enclosed by the eyelashes scales as $1/2\rho u_z^2(z = L)$, where ρ is the air density, and $u_z(z = L)$ is the vertical air velocity entering the eyelash array at $z = L$, following equation (2.3). This incoming air flows over the ocular surface and through the eyelash array. Energy is lost to viscous dissipation via shear stresses on the ocular surface and eyelashes before flowing out of the eyelash array. The shear stress τ_2 at the ocular surface is given as $\tau_2 = \mu U_2/\delta$, by assuming the boundary layer thickness is equal to that for the case without lashes. The pressure (and energetic) loss ΔP for flowing through the eyelash array follows lubrication flow theory for flow through a linear array of cylinders [14,15], as outlined in §2.6 and equation (2.4). The kinetic energy of the airflow leaving the eyelash array can be expressed as $\frac{1}{2}\rho U_2^2$. The energy balance between the flow entering and leaving the eyelash array yields an expression that can be evaluated to determine the radial airflow velocity U_2 leaving the eyelash array, or $\frac{1}{2}\rho u_z^2(z = L) = \tau_2(U_2) + \Delta P(U_2) + \frac{1}{2}\rho U_2^2$.

The kinetic energy $\frac{1}{2}\rho U_2^2$ leaving the eyelash array was found to be negligible compared with the other terms, so the kinetic energy entering the eyelash array is balanced by the shear stress at the eye surface τ_2 and the pressure (energetic) loss ΔP through the eyelash array, or $\frac{1}{2}\rho u_z^2(z = L) = \tau_2(U_2) + \Delta P(U_2)$. Following this expression, we can determine the radial velocity U_2 to be, $U_2 = (2\rho(aL)^2)/(\mu[((S - d)D/S^2) + 1/\delta])$, where D is the dimensionless drag given as $D = 9\pi/2^{3/2}(1 - d/S)^{5/2} = 9\pi/2^{3/2}\phi^{5/2}$. We can then use this velocity to determine the shear stress τ_2 at the ocular surface, or

$$\tau_2 = \frac{2\rho(aL)^2}{\delta[((S - d)D)/S^2 + 1/\delta]}. \tag{3.5}$$

The shear stress for a lash of arbitrary length L is a combination of the two shear stresses τ_1 and τ_2. When lashes are short, the term τ_1 dominates as $\tau_1 \sim L^{-1}$; conversely, when lashes are long, the term τ_2 dominates as $\tau_2 \sim L^2$. By combining these two terms, we get an expression for the shear stress τ at the eye surface for a given eyelash length L, or

$$\tau = \frac{\mu a W}{\delta + 4L} + \frac{2\rho(aL)^2}{\delta[(S - d)D/S^2 + 1/\delta]}. \tag{3.6}$$

Figure 8*a* shows the relation between eyelash length L/W and normalized shear stress $\bar{\tau}$, which is the shear stress τ divided by the shear stress τ_0 of an eye without eyelashes. Results correspond to mammalian eyelashes with thickness $d = 100$ µm. We see that for the porosity range found in nature, $\phi = 0.5$–0.8, there exists a minimum value for shear stress at intermediate eyelash lengths of $L/W = 0.21$–0.39. These lengths are similar to those found in nature in §3.1 and equation (3.2).

3.3. Numerical simulation

We use numerical simulations to investigate the velocity field around the eyelashes and compare it to our scaling model. Velocity profiles for our theoretical predictions are given in figure 7*b*–*d* and for our numerical results given in figure 7*e*–*g*. The streamlines associated with our numerical results are given in figure 7*h*–*j*. Only half the flow is shown because streamlines are axisymmetric around the centre of the eye.

Figure 7*e*,*h* shows the flow profile and streamlines for an eye with no lashes, typical of sufferers of madarosis. The flow profile is consistent with theoretical solutions for a viscous flow near a stagnation point, where successive streamlines veer horizontally as they approach the eye [12]. The flow profile is parabolic as expected. The slope of the dashed line indicates the inverse of the shear rate $\dot{\gamma}^{-1}$ at the ocular surface. The shear stress τ is proportional to the shear rate $\dot{\gamma}$ following $\tau = \mu\dot{\gamma}$.

The presence of lashes alters both the streamlines and the flow profile compared with the baseline case of no lashes. For optimal eyelashes, a stagnation zone created by the eyelashes shields the eye and forces air to travel above instead of penetrating through the eyelashes. This shielding effect is consistent with the shear stress τ found through scaling analyses, as shown by the first term in equation (3.6). The stagnation zone acts to thicken the boundary layer above the ocular surface, and so decrease both shear stress τ and shear rate $\dot{\gamma}$. For instance, in the streamlines for optimal lashes in

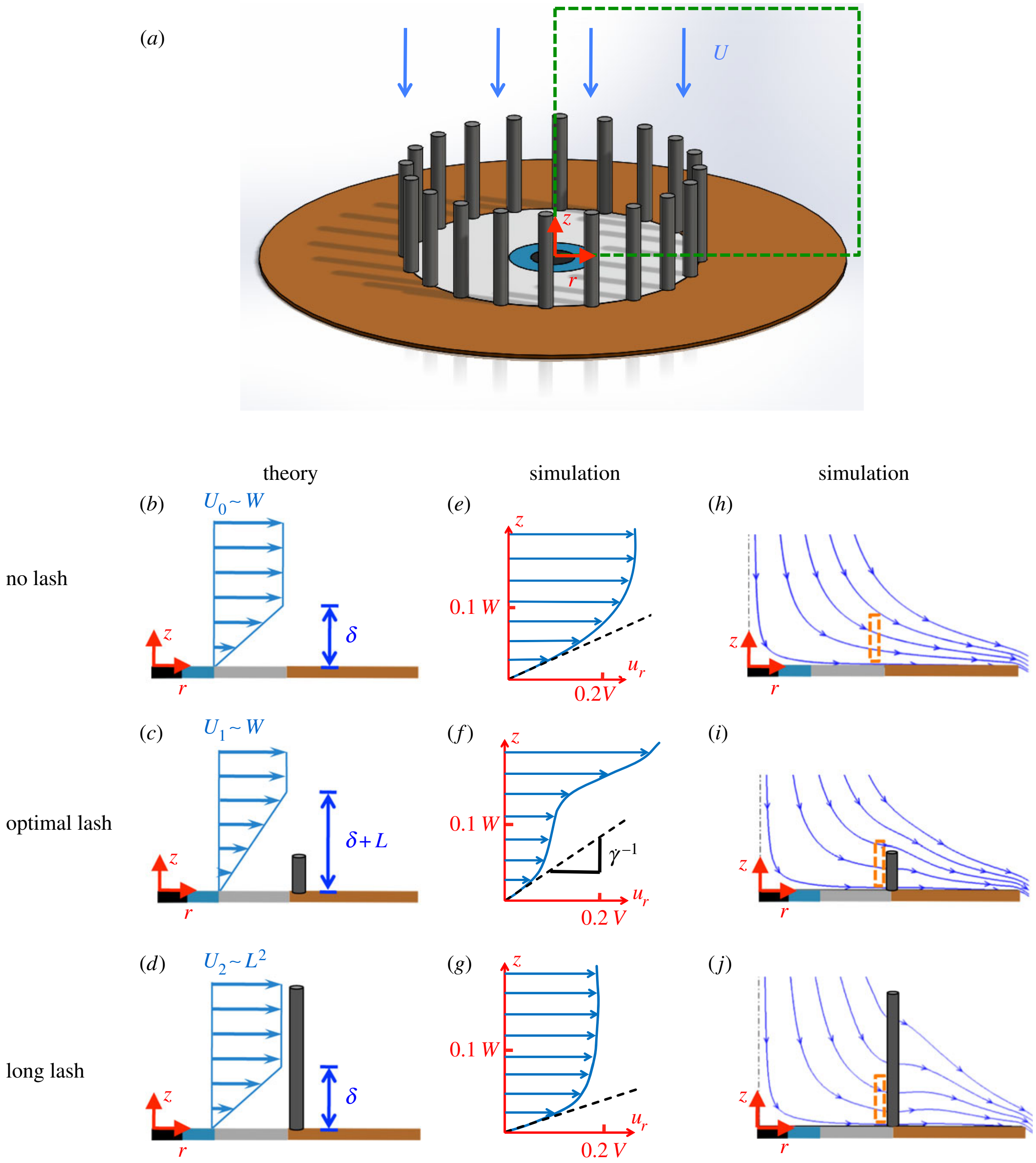

Figure 7. Velocity near the eye. (*a*) Dashed box shows cross section of flow from which velocity is shown. Columns show both theoretical (*b*–*d*) and (*e*–*g*) numerical predictions for the radial velocity u_r distribution along the height z above the ocular surface. (*h*–*j*) The final column shows numerical predictions for streamlines. The dashed box shows the location of the velocity profiles in (*e*–*g*). Rows represent the three cases: no lashes, optimal lashes and long lashes. (Online version in colour.)

figure 7*i*, we note a 'bump', which corresponds to the incoming flow turning earlier than in the case of no lashes and long lashes.

By comparing the velocity profiles in figure 7*e*,*f*, we see that flow speed near the ocular surface for an optimal eyelash, $L/W = 0.2$, is half that of an eye without lashes, indicating a thicker boundary layer. This low speed is associated with lower shear rate $\dot{\gamma}$ and shear stress τ on the ocular surface. Moreover, when comparing the streamlines, we see that the streamlines close to the eye for optimal lashes are farther apart than those for no lashes and long lashes. The distance between streamlines corresponds to flow rate; closer spaced streamlines signify greater flow rate [11]. The increased flow rate for long lashes is consistent with our scaling theory, which predicts high flow speeds U_2 for longer lashes since $U_2 \sim L^2$.

In figure 8*b*, we see how normalized shear rate $\bar{\dot{\gamma}}$ varies with eyelash length L/W. Normalized shear rate $\bar{\dot{\gamma}}$ is the shear rate $\dot{\gamma}$ divided by the shear rate $\dot{\gamma}_0$ without lashes present. By comparing figure 8*a*–*b*, we see qualitatively similar relationships between the shear stress τ, equation (3.6), found theoretically, and the shear rate $\dot{\gamma}$, found numerically. Both shear stress τ and shear rate $\dot{\gamma}$ vary nonlinearly with eyelash length, with a minimum value at an intermediate eyelash length $L/W \approx 0.2$.

3.4. Wind tunnel experiments

We use our wind tunnel to measure the effect of eyelash length and porosity on flow across an ocular surface. The ocular surface in our experiments is a 2-cm dish filled with 0.6 ml of water, whose evaporation rate $\dot{m}$ is measured

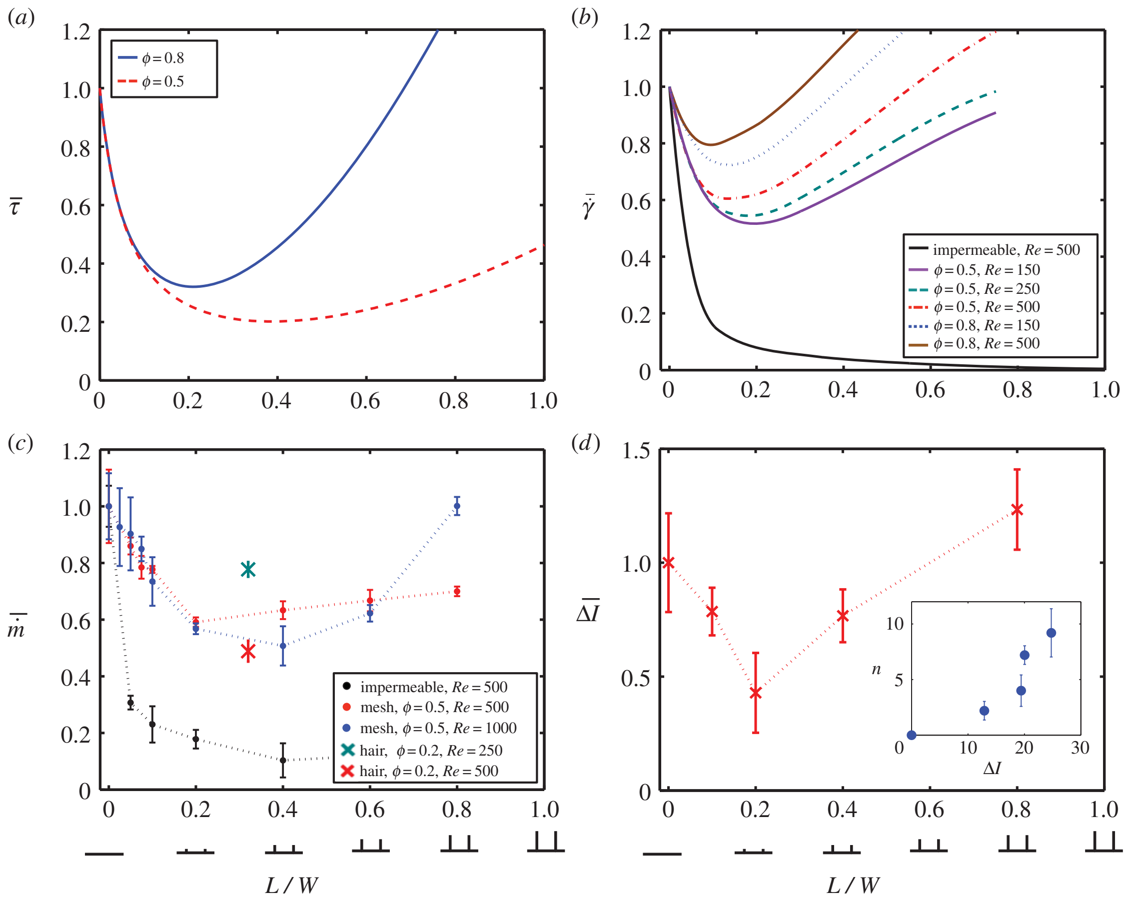

Figure 8. (*a*) Shear stress $\bar{\tau}$, (*b*) shear rate $\bar{\dot{\gamma}}$, (*c*) evaporation rate $\bar{\dot{m}}$, and (*d*) change in fluorescence intensity $\overline{\Delta I}$, all versus eyelash length *L/W*. All values reported are normalized with their respective values for an eye with no lashes. (*d*) Inset shows relationship between number of deposited drops *n* in drops mm^{-2} and change in fluorescence intensity ΔI. (Online version in colour.)

using an analytical balance. The speed of the wind tunnel is set to ensure aerodynamic similitude with the laminar flow around the eye of animals walking ($Re = 500$–1000). We test three types of eyelash-mimics, those constructed with human hair, wire mesh and impermeable paperboard.

Figure 8*c* shows the relation between eyelash length L/W and normalized evaporation rate $\bar{\dot{m}}$, which is the evaporation rate $\dot{m}$ divided by the evaporation rate $\dot{m}_0$ of a dish without eyelashes. The black points show the evaporation rate for impermeable paperboard with porosity $\phi = 0$, similar to a lens shade used to reduce glare in photography. In this case, evaporation rate decreases monotonically with the paperboard height, as expected. While effective in reducing flow, such a lens shade would be of little use to animals because it would obscure vision and be difficult to clean.

The red and blue data points in figure 8*c* show evaporation rates for the mesh of porosity $\phi = 0.5$ subjected to flows of $Re = 500$ and 1000, respectively. The optimal eyelash length $L/W = 0.3 \pm 0.1$ that minimizes evaporation agrees with our measurements of animal eyelashes.

To determine the eyelashes' effect on deposited particles, we attach a commercial humidifier to our wind tunnel to inject fluorescent drops with an average diameter of 10 µm, and so generate a particle-laden flow. An absorbent paper disc is placed on the ocular surface to intercept incoming drops. Figure 2*b* shows fluorescent drops deposited onto the eye mimic both before and after 10 min of testing. As shown in the inset of figure 8*d*, higher fluorescence intensity corresponds to a greater number of drops deposited. In addition to reducing evaporation, eyelashes significantly reduce deposition of drops, as shown in figure 8*d*. An optimal eyelash length of $L/W = 0.25 \pm 0.15$ is found, which is consistent with our evaporation results.

The trends found in evaporation and deposition experiments are similar to those found by numerical simulation. The largest Reynolds number we can simulate is 500, which is half of the maximum Reynolds number used in the experiments. For convenience, we choose shear rate $\dot{\gamma}$, averaged across the eye surface, as the single metric to characterize the flow. This value is indicative of eyelash performance because lower shear rate is associated both with lower particle deposition [49] and reduced evaporation [50]. The curves in figure 8*b* show the normalized shear rate $\bar{\dot{\gamma}}$ from simulation for a range of Reynolds number for medium-sized animals, $Re = 150$–500, and porosities $\phi = 0.5$ and 0.8. While the absolute values vary with Reynolds number and porosity, all simulations indicate the presence of an optimal eyelash length at $L/W = 0.2$, as is consistent with our evaporation rate and deposition experiments.

To determine the universality of the optimal value, we conduct a series of five evaporation experiments and 10 simulations using porosities of $\phi = 0.5$–0.8, and Reynolds numbers $Re = 30$–1000. Combining these results yields a relation between Reynolds number and optimal eyelash lengths, given in figure 9. The cyan triangles show the measured dimensionless eyelash lengths for mammals, whereas the red

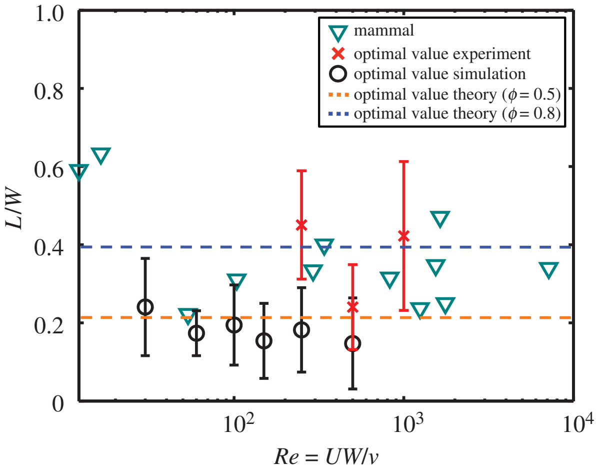

Figure 9. Relationship between eyelash length L/W and Reynolds number. Measurements of animal eyelashes are shown alongside optimal values obtained from simulations, experiments and scaling theory. The vertical bars represent the range of eyelash lengths within 10% of their optimal values, estimated by a spline curve-fitting of the experimental and numerical data. (Online version in colour.)

points refer to experiments, the black points to simulations and the dashed lines to theory. All mammals remain within a close range ($L/W = 0.4 \pm 0.2$), as do the results for experiments ($L/W = 0.4 \pm 0.2$), simulations ($L/W = 0.20 \pm 0.15$) and aerodynamic scaling theory ($L/W = 0.3 \pm 0.09$). Among the mammals, we observe that the optimal eyelash length is conserved across sizes, from a hedgehog to a giraffe.

4. Discussion

Eyelashes, previously known as mechanical sensors and sunshades, are shown in this study to act as air filters for the eye. However, they act differently from other filtering systems in the body such as hairs in the nose and airway, which act as ram filters, trapping particles that are impacted into the hairs. One detriment to such systems, as with synthetic HVAC systems, is that they must be cleaned periodically to remove particles and permit air to flow, normally through the act of sneezing. By contrast, eyelashes do not collect particles, but instead redirect flows. When dirty, their flexibility and porosity facilitates cleaning simply by brushing or rinsing with water. Furthermore, their porosity facilitates passage of light, critical to the eye's function. Our simulations show that lower eyelash porosity decreases the magnitude of shear rate; however, the optimal length of lashes remains independent of porosity. A balance between reducing visual obstruction and airflow at the eye surface is likely to result in the range of eyelash densities shown in figure 5.

Because eyelashes act so differently to typical filters, they may have application in places that are difficult or costly to clean regularly. Applications aimed at reducing dust deposition onto sensitive sensors or solar panels may benefit from strategically placed eyelash-inspired filaments to keep surfaces clean while minimally obscuring light. Photovoltaic solar panels suffer a major problem of particle accumulation, which reduces their efficiency by 6% annually [51]. Currently, transparent electrodynamic coatings are being developed to prevent dust accumulation through the pulsing of electric currents [52–54]. Dust accumulation is also important for the maintenance of remote-sensing applications, such as for autonomous robots, which cannot be easily accessed once deployed [53,54].

Can people use the ideas from this study to prevent infection of the eye? False eyelashes are quite common in the cosmetics industry, but their effect on health is unknown. The human-hair eyelashes, shown in figure 2*a*, tested in our experiments represent typical false eyelashes used by people to accentuate their eyes. The evaporation rates found from these experiments, represented by the crosses in figure 8*a*, were higher than expected for such low porosity, $\phi = 0.2$. This can be attributed to their curvature, which guides more air towards the eye surface. The increase of air flow at the eye surface caused by the curvature of false eyelashes negates the effects of their low porosity, resulting in evaporation rates comparable to the synthetic mesh with a porosity of $\phi = 0.5$, typical for humans. Although we still expect the optimal eyelash length to hold for false eyelashes, their high curvature increases the magnitude of evaporation at the eye surface and so reduces the shielding effect. Thus, wearing curved false eyelashes of low porosity can potentially provide extra protection to the eye and reduce dry eye.

We observed the red kangaroo and giraffe having multiple rows of eyelashes. These two mammal species live in dusty, arid environments, where airborne particle deposition can be substantial. Having multiple rows increases the density ρ_{lash} of eyelashes, and so decreases their porosity ϕ. From our simulation, we see that a decrease in porosity ϕ results in a decrease in the magnitude of shear stress, causing less airflow to reach the eye surface. Another notable adaptation to dry, dusty environments is the translucent eyelids of camels, used to weather dust storms [55].

Animals in dusty environments may squint or partially close their eyes in response to wind and dust. Squinting decreases the exposed area of the eye, and so decreases the rate of evaporation. However, it also increases the dimensionless length of the lashes L/W, relatively increasing evaporation and deposition. The competition between these two factors will determine whether squinting is beneficial.

We made a series of geometrical simplifications in our study, which may affect the accuracy of our results. We performed experiments with a flat, circular eye with eyelashes of uniform length. In reality, eyes are three-dimensional with curved surfaces, non-circular openings and eyelashes of varying lengths. However, we expect our results to hold qualitatively because the main attribute affecting flow at the eye surface is the porosity of the eyelash array. In this study, we focused on the eye facing normally to the incoming flow. This configuration is the most dangerous with respect to evaporation and contamination of the eye [50]. As flows outside of this configuration occur regularly in nature, we also investigated the effect of varying flow direction. In particular, we tilted the eye 20° from the normal direction and find that an optimal eyelash length around $L/W = 0.2$ still exists, but with 50% reduction in protective benefits.

In our analysis, we modelled our airflows according to those experienced by mammals during walking locomotion, for which the aerodynamics are in a laminar flow regime. For running gaits, the global Reynolds number $Re = UW/\nu$ is in the transition regime so may be considered turbulent. Our experiments, simulations and model are only valid for laminar flow regimes.

Birds have also been observed to possess lash-like feathers around their eyes [6]. At the American Museum of Natural History, we measured the 'eyelash' length L and eye opening width W for four different bird species and found that these species did not follow the trend found for mammals, equation (3.2). Instead, we find that $L/W = 0.86$ with $R^2 = 0.76$. The difference in trends may be due to the turbulent flow regime experienced by birds during flight.

Eyelash flexibility and curvature have a negligible influence on our results. We perform three simulations using the characteristic radius of curvature of the human eyelash, $0.5L$. The results were consistent with those found for straight lashes and were included in the simulation results for figure 9. We also find eyelashes are effectively rigid when exposed to flow associated with the Reynolds number of the anteater, lemur, opossum, chimpanzee, snow leopard, cougar, tapir, wild boar, red kangaroo and wild sheep during their walking gait of locomotion. The ratio of viscous to elastic forces [56] is $(256\mu L^3 V)/Ed^4 \ln(2L/d) \sim 10^{-3} - 10^{-5}$, where $E \approx 9$ GPa is the modulus of elasticity of eyelashes [57]; the ratio of inertial and elastic forces [58] is $\rho V^2 L^3/Ed^3 \sim 10^{-3} - 10^{-8}$, indicating typical air flow has a negligible effect on eyelash deflection.

Finally, eyes are dynamic systems that blink, tear and move. Such systems may be used to compensate for the observed variability in eyelash length and density (e.g. figure 4*b*). The effects from these active strategies are worth investigating in the context of preventing tear film evaporation and contamination. Experiments involving *in vivo* measurements of tear film evaporation of mammalian species with variable eyelash lengths may provide insight into the implementation of dynamic mechanisms to protect the eye.

5. Conclusion

Our study demonstrates that eyelashes divert airflows, acting as a passive dust controlling system for the eyes. They reduce evaporation and particle deposition up to 50%, indicating the evolution of eyelashes may have played a role in reducing the frequency of endogenous blinks, which replenish and clean the tear film [2]. Our experiments show that eyelashes of an intermediate length accrue the greatest benefits in terms of flow reduction and particle deposition. In our simulations, the optimum eyelash length is assessed through shear rate as a proxy for particle deposition and evaporation. This optimum is unique to porous eyelashes, and does not apply for completely impermeable eyelashes, such as paper cylinders. Thus the porosity of surfaces can induce non-intuitive and advantageous flows. Through scaling, we find that the optimum arises because the aerodynamic drag imposed by short eyelashes thickens the boundary layer above the ocular surface, while long lashes channel flow with high kinetic energy towards the ocular surface. As a result, the shear stress at the eye surface scales as the inverse of eyelash length, or $\tau \sim L^{-1}$, for short lashes; shear stress scales with eyelash length squared, or $\tau \sim L^2$, for long lashes. The combination of these two competing effects gives rise to an optimum length for eyelashes that minimizes shear stress, shear rate, evaporation and contamination at the ocular surface. We find the optimal eyelash length to be $L/W = 0.35 \pm 0.15$, following anatomical measurements, aerodynamic scaling analysis, numerical simulation and wind tunnel experiments.

Acknowledgements. We thank F. Chen and K. Vistarakula for their early contributions.

Funding statement. We thank financial support of the NSF (PHY-1255127 and CBET-1256403).

References

1. Bielory L, Friedlaender MH. 2008 Allergic conjunctivitis. *Immunol. Allergy Clin. North Am.* **28**, 43–58. (doi:10.1016/j.iac.2007.12.005)
2. Braun RJ. 2012 Dynamics of the tear film. *Annu. Rev. Fluid Mech.* **44**, 267–297. (doi:10.1146/annurev-fluid-120710-101042)
3. Friedlaender MH. 1995 A review of the causes and treatment of bacterial and allergic conjunctivitis. *Clin. Ther.* **17**, 800–810. (doi:10.1016/0149-2918(95)80058-1)
4. Gong S, Zhou Q, LeDoux MS. 2003 Blink-related sensorimotor anatomy in the rat. *Anat. Embryol.* **207**, 193–208. (doi:10.1007/s00429-003-0341-6)
5. Cohn JF, Xiao J, Moriyama T, Ambadar Z, Kanade T. 2003 Automatic recognition of eye blinking in spontaneously occurring behavior. *Behav. Res. Methods Instrum. Comput.* **35**, 420–428. (doi:10.3758/BF03195519)
6. Martin G, Coetzee H. 2004 Visual fields in hornbills: precision-grasping and sunshades. *Ibis* **146**, 18–26. (doi:10.1111/j.1474-919X.2004.00211.x)
7. American Optometric Association. 2011 *Care of the patient with ocular surface disorders*. St Louis, Mo: American Optometric Association.
8. Levy Y, Segal N, Ben-Amitai D, Danon Y. 2004 Eyelash length in children and adolescents with allergic diseases. *Pediatr. Dermatol.* **21**, 534–537. (doi:10.1111/j.0736-8046.2004.21501.x)
9. Johnstone MA, Albert DM. 2002 Prostaglandin-induced hair growth. *Survey Opthalmol.* **47**, S185–S202. (doi:10.1016/S0039-6257(02)00307-7)
10. Dickerson AK, Mills ZG, Hu DL. 2012 Wet mammals shake at tuned frequencies to dry. *J. R. Soc. Interface* **9**, 3208–3218. (doi:10.1098/rsif.2012.0429)
11. Panton RL. 2005 *Incompressible flow.* Hoboken, NJ: John Wiley & Sons.
12. Schlichting H. 1955 *Boundary-layer theory*. New York, NY: McGraw-Hill.
13. Hiemenz K. 1911 Die Grenzschicht an einem in den gleichförmigen Flüssigkeitsstrom eingetauchten geraden Kreiszylinder. *Dinglers Polytechnisches J.* **326**, 321–324.
14. Keller JB. 1964 Viscous flow through a grating or lattice of cylinders. *J. Fluid Mech.* **18**, 94–96. (doi:10.1017/S0022112064000064)
15. Ayaz F, Pedley T. 1999 Flow through and particle interception by an infinite array of closely spaced circular cylinders. *Eur. J. Mech. B/Fluids* **18**, 173–196. (doi:10.1016/S0997-7546(99)80021-1)
16. Succi S. 2001 *The lattice boltzmann equation: for fluid dynamics and beyond*. Oxford, UK: Oxford University Press.
17. Aidun CK, Clausen JR. 2010 Lattice-Boltzmann method for complex flows. *Annu. Rev. Fluid Mech.* **42**, 439–472. (doi:10.1146/annurev-fluid-121108-145519)
18. Ladd A, Verberg R. 2001 Lattice-Boltzmann simulations of particle-fluid suspensions. *J. Stat. Phys.* **104**, 1191–1251. (doi:10.1023/A:1010414013942)
19. Mills ZG, Mao W, Alexeev A. 2013 Mesoscale modeling: solving complex flows in biology and biotechnology. *Trends Biotechnol.* **31**, 246–434. (doi:10.1016/j.tibtech.2013.05.001)
20. Gauger E, Stark H. 2006 Numerical study of a microscopic artificial swimmer. *Phys. Rev. E* **74**, 021907. (doi:10.1103/PhysRevE.74.021907)
21. Jian H, Vologodskii AV, Schlick T. 1997 A combined wormlike-chain and bead model for dynamic simulations of long linear DNA. *J. Comput. Phys.* **136**, 168–179. (doi:10.1006/jcph.1997.5765)
22. Clift R, Grace JR, Weber ME. 2005 *Bubbles, drops, and particles*. Mineola, NY: Courier Dover Publications.
23. Peskin CS. 2002 The immersed boundary method. *Acta Numer.* **11**, 479–517. (doi:10.1017/S0962492902000077)
24. Bouzidi M, Firdaouss M, Lallemand P. 2001 Momentum transfer of a Boltzmann-lattice fluid

with boundaries. *Phys. Fluids* **13**, 3452. (doi:10.1063/1.1399290)

25. Lamb H. 1993 *Hydrodynamics*. Cambridge, UK: Cambridge University Press.
26. Finn R. 1953 Determination of the drag on a cylinder at low Reynolds numbers. *J. Appl. Phys.* **24**, 771–773. (doi:10.1063/1.1721373)
27. Proudman I, Pearson J. 1957 Expansions at small Reynolds numbers for the flow past a sphere and a circular cylinder. *J. Fluid Mech.* **2**, 237–262. (doi:10.1017/S0022112057000105)
28. Ghosh R, Buxton GA, Usta OB, Balazs AC, Alexeev A. 2009 Designing oscillating cilia that capture or release microscopic particles. *Langmuir* **26**, 2963–2968. (doi:10.1021/la902926w)
29. Branscomb J, Alexeev A. 2010 Designing ciliated surfaces that regulate deposition of solid particles. *Soft Matter* **6**, 4066–4069. (doi:10.1039/c0sm00185f)
30. Semmler C, Alexeev A. 2011 Designing structured surfaces that repel fluid-borne particles. *Phys. Rev. E* **84**, 066303. (doi:10.1103/PhysRevE.84.066303)
31. Mills ZG, Aziz B, Alexeev A. 2012 Beating synthetic cilia enhance heat transport in microfluidic channels. *Soft Matter* **8**, 11 508–11 513. (doi:10.1039/c2sm26919h)
32. Masoud H, Alexeev A. 2010 Resonance of flexible flapping wings at low Reynolds number. *Phys. Rev. E* **81**, 056304. (doi:10.1103/PhysRevE.81.056304)
33. Kilimnik A, Mao W, Alexeev A. 2011 Inertial migration of deformable capsules in channel flow. *Phys. Fluids* **23**, 123302. (doi:10.1063/1.3664402)
34. Mao W, Alexeev A. 2014 Motion of spheroid particles in shear flow with inertia. *J. Fluid Mech.* **749**, 145–166. (doi:10.1017/jfm.2014.224)
35. Yeh PD, Alexeev A. 2014 Free swimming of an elastic plate plunging at low Reynolds number. *Phys. Fluids* **26**, 053604. (doi:10.1063/1.4876231)
36. Munson BR, Young DF, Okiishi TH. 1990 *Fundamentals of fluid mechanics.* Hoboken, NJ: John Wiley & Sons.
37. Wroot AJ. 1984 *Feeding ecology of the European hedgehog* Erinaceus europaeus. Royal Holloway, UK: University of London.
38. Seipel S, Seipel T. 2008 *Giant anteaters*. Minneapolis, MN: Lerner Publications.
39. O'Neill MC. 2012 Gait-specific metabolic costs and preferred speeds in ring-tailed lemurs (*Lemur catta*), with implications for the scaling of locomotor costs. *Am. J. Phys. Anthropol.* **149**, 356–364. (doi:10.1002/ajpa.22132)
40. Parchman AJ, Reilly SM, Biknevicius AR. 2003 Whole-body mechanics and gaits in the gray short-tailed opossum *Monodelphis domestica*: integrating patterns of locomotion in a semi-erect mammal. *J. Exp. Biol.* **206**, 1379–1388. (doi:10.1242/jeb.00267)
41. San Diego Zoo. 2011 Giant panda, *Ailuropoda melanoleuca*. See http://library.sandiegozoo.org/factsheets/giant_panda/panda.htm.
42. Sockol MD, Raichlen DA, Pontzer H. 2007 Chimpanzee locomotor energetics and the origin of human bipedalism. *Proc. Natl Acad. Sci. USA* **104**, 12 265–12 269. (doi:10.1073/pnas.0703267104)
43. Dumont B, Dutronc A, Petit M. 1998 How readily will sheep walk for a preferred forage? *J. Anim. Sci.* **76**, 965–971.
44. Yousef M, Webster M, Yousef O. 1989 Energy costs of walking in camels, *Camelus dromedarius*. *Physiol. Zool.* **62**, 1080–1088.
45. Eisenhauer JG. 2003 Regression through the origin. *Teach. Stat.* **25**, 76–80. (doi:10.1111/1467-9639.00136)
46. Bininda-Emonds OR *et al*. 2007 The delayed rise of present-day mammals. *Nature* **446**, 507–512. (doi:10.1038/nature05634)
47. Felsenstein J. 1985 Phylogenies and the comparative method. *Am. Nat.* **125**, 1–15. (doi:10.1086/284325)
48. Garland T, Bennett AF, Rezende EL. 2005 Phylogenetic approaches in comparative physiology. *J. Exp. Biol.* **208**, 3015–3035. (doi:10.1242/jeb.01745)
49. Schneider T, Bohgard M. 2005 Airborne particle deposition onto the ocular surface. *Indoor Air* **15**, 215–219. (doi:10.1111/j.1600-0668.2005.00350.x)
50. Bergman TL, Incropera FP, Lavine AS, DeWitt DP. 2011 *Fundamentals of heat and mass transfer.* Hoboken, NJ: John Wiley & Sons.
51. Kumar ES, Sarkar B. 2013 Soiling and dust impact on the efficiency and the maximum power point in the photovoltaic modules. *Int. J. Eng.* **2**, 1–8.
52. Sims R, Biris A, Wilson J, Yurteri C, Mazumder M, Calle C, Buhler C. 2003 Development of a transparent self-cleaning dust shield for solar panels. In *Proc. ESA-IEEE Joint Meeting on Electrostatics*, pp. 814–821. Cambria, CA: Laplacian Press.
53. Mazumder M, Biris A, Sims R, Calle C, Buhler C. 2003 Solar panel obscuration in the dusty atmosphere of mars. In *Proc. ESA-IEEE Joint Meeting on Electrostatics*, pp. 208–288. Cambria, CA: Laplacian Press.
54. Calle C *et al*. 2008 Dust particle removal by electrostatic and dielectrophoretic forces with applications to NASA exploration missions. In *Proc. Electrostatics Society of America Annual Meeting, Minneapolis*, pp. 17–19. Cambria, CA: Laplacian Press.
55. Morton R. 1984 Camels for meat and milk production in Sub-Sahara Africa. *J. Dairy Sci.* **67**, 1548–1553. (doi:10.3168/jds.S0022-0302(84)81477-0)
56. Guglielmini L, Kushwaha A, Shaqfeh ES, Stone HA. 2012 Buckling transitions of an elastic filament in a viscous stagnation point flow. *Phys. Fluids* **24**, 123601. (doi:10.1063/1.4771606)
57. Goldsmith LA, Baden HP. 1971 The mechanical properties of hair II. Chemical modifications and pathological hairs. *J. Invest. Dermatol.* **56**, 200–204. (doi:10.1111/1523-1747.ep12260826)
58. de Langre E. 2008 Effects of wind on plants. *Annu. Rev. Fluid Mech.* **40**, 141–168. (doi:10.1146/annurev.fluid.40.111406.102135)